# Shaping highly regular glass architectures: A lesson from nature

Vanessa Schoeppler, Elke Reich, Jean Vacelet, Martin Rosenthal, Alexandra Pacureanu, Alexander Rack, Paul Zaslansky, Emil Zolotoyabko, Igor Zlotnikov

CRYSTAL STRUCTURE

# Shaping highly regular glass architectures: A lesson from nature

Vanessa Schoeppler,[1] Elke Reich,[1] Jean Vacelet,[2] Martin Rosenthal,[3] Alexandra Pacureanu,[3] Alexander Rack,[3] Paul Zaslansky,[4] Emil Zolotoyabko,[5] Igor Zlotnikov[1]*



**Demospongiae is a class of marine sponges that mineralize skeletal elements, the glass spicules, made of amorphous silica. The spicules exhibit a diversity of highly regular three-dimensional branched morphologies that are a paradigm example of symmetry in biological systems. Current glass shaping technology requires treatment at high temperatures. In this context, the mechanism by which glass architectures are formed by living organisms remains a mystery. We uncover the principles of spicule morphogenesis. During spicule formation, the process of silica deposition is templated by an organic filament. It is composed of enzymatically active proteins arranged in a mesoscopic hexagonal crystal-like structure. In analogy to synthetic inorganic nanocrystals that show high spatial regularity, we demonstrate that the branching of the filament follows specific crystallographic directions of the protein lattice. In correlation with the symmetry of the lattice, filament branching determines the highly regular morphology of the spicules on the macroscale.**

## INTRODUCTION

Marine sponges (phylum Porifera) represent one of the oldest multicellular metazoan groups whose fossil record stretches back, more than half a billion years, to the Neoproterozoic (*1*, *2*). Demospongiae and Hexactinellida, two classes of sponges, synthesize mineralized siliceous skeletal elements, glass spicules, which provide the animals with structural support and mechanical strength and help protect them from their environment. The spicules, made of hydrated amorphous silica, are typically divided into two categories according to their relative size and role in the skeleton, that is, megascleres and microscleres (*3*). The latter exhibit a fascinating diversity of the most intricate species-specific three-dimensional (3D) morphologies displaying high spatial regularity and symmetry (Fig. 1) (*4*, *5*). Whether the spicules have a simple elongated needle-like shape (Fig. 1A) or branch to form a tetrapod-like or a star-like morphology (Fig. 1B) or even in the case of complex sphere-like spicules consisting of multiple rays originating from the center (Fig. 1D), all branches of the spicules harbor a proteinaceous axial filament (*6*). The filament, up to 3 μm in diameter, is predominantly composed of spatially ordered enzymatically active proteins, silicatein and its derivatives, which catalyze silica biofabrication and act as a template for its deposition (*7*). The exact process of spicule formation, which proceeds with the involvement of specialized cells (the sclerocytes), is still under debate (*8*). Nevertheless, it is well accepted that axial filaments play an essential role in directing the process of silica biomineralization and thus governing the morphogenesis of sponge spicules (*9*, *10*). However, precisely what guides the 3D morphology of the axial filament itself remains an open question.

The highly regular ordering of proteins inside the axial filaments in spicules of both Demospongiae and Hexactinellida, revealing a hexagonal or tetragonal symmetry, respectively, was previously observed using different electron microscopy techniques and x-ray analysis (*11*–*19*). Consequently, in cross section, the filaments in Demospongiae typically look like a derivative of a hexagonal shape (such as hexagon-like and triangle-like and shapes in-between) (*11*, *17*, *19*), whereas the filaments in Hexactinellida are characteristically square-shaped (*11*, *14*, *16*). On the basis of these observations, we hypothesize a critical relationship between the crystal-like nature of the axial filaments in siliceous sponges and the spatial morphology of the spicules on the macroscale. We suggest that the lattice symmetry of the filament determines its branching behavior that follows specific crystallographic directions. Ultimately, this guides the symmetry of the spicules. A similar synthesis approach of highly regular man-made inorganic nanocrystals is currently under fast development (*20*–*25*). Rod-like, regular multipods and hyperbranched crystals are synthesized from a large variety of materials, such as metals, metal oxides, and semiconductors. In these structures, the branching occurs on specific crystallographic planes. For example, gold (face-centered cubic) (*21*) and selenium (hexagonal) (*20*) can form a variety of planar perfectly symmetric multipods while maintaining a single crystal-like nature. CdSe and CdTe have been shown to form either single-crystalline rods or highly regular tetrapods, consisting of cubic (zinc-blende) nuclei with {111} facets, each projecting a hexagonal (wurtzite-type) arm, or hyperbranched spherical structures, depending on growth conditions (*24*, *25*). Here, we apply similar considerations to explain spiculogenesis in sponges from the class Demospongiae based on the symmetry of the protein crystal comprising their axial filaments.

## RESULTS

We analyzed three types of spicules with increasing levels of spatial complexity taken from three different sponges. First are needle-shaped megascleres from the sponge *Tethya aurantium* (Pallas, 1766) known as strongyloxea (Fig. 1A). These spicules, arranged in bundles that radiate from the center of this subspherical sponge, can reach a diameter of 35 μm and a length of 2 mm (*26*, *27*). In accordance with the hexagonal lattice of the proteinaceous axial filament in demosponges, its morphology in cross section exhibits a sixfold symmetry and, in some instances, appears as a perfect hexagon (inset in Fig. 1A). The second type of spicules that we analyzed are megascleres from the sponge *Stryphnus ponderosus* (Bowerbank, 1866) called dichotriaenes (Fig. 1B). These spicules exhibit a highly regular shape that has a basic form of a tetrapod

[1]B CUBE–Center for Molecular Bioengineering, Technische Universität Dresden, Dresden, Germany. [2]IMBE (Institut Méditerranéen de Biodiversité et d'Écologie marine et continentale), CNRS, Aix-Marseille Université, Université d'Avignon, IRD (Institut de Recherche pour le Développement), Station Marine d'Endoume, Marseille, France. [3]European Synchrotron Radiation Facility, Grenoble, France. [4]Julius Wolff Institute for Biomechanics and Musculoskeletal Regeneration, Berlin, Germany. [5]Department of Materials Science and Engineering, Technion, Haifa, Israel.
*Corresponding author. Email: igor.zlotnikov@tu-dresden.de

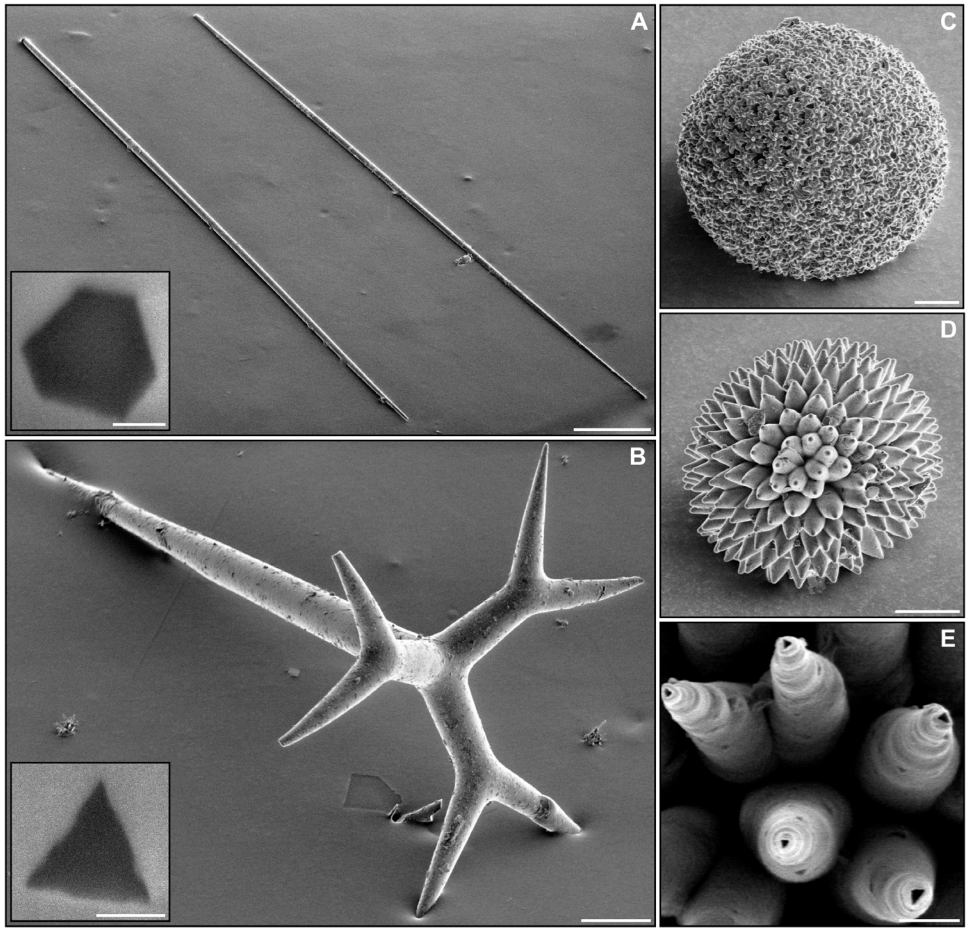


**Fig. 1. The morphology of demosponge spicules and their inner axial filaments as revealed by scanning electron microscopy.** (**A**) Megascleres from the demosponge *T. aurantium*. Scale bar, 100 μm. Inset: Cross section of the spicule obtained by focused ion beam (FIB). Scale bar, 1 μm. (**B**) Megasclere from the demosponge *S. ponderosus*. Scale bar, 100 μm. Inset: Cross sections of the main shaft of the spicule obtained by FIB. Scale bar, 1 μm. Note: Some spicule tips were broken during sample preparation and appear to be flat. (**C** to **E**) Microscleres from the demosponge *G. cydonium* at different maturation levels, from a fully mature spicule to an immature one, respectively. Scale bars, 10 μm (C), 10 μm (D), and 1 μm (E).

with three arms (cladome) radiating from the main shaft (rhabdome). Each arm splits into two additional branches. They are confined to the cortex of the sponge, with the cladome at the sponge periphery and the rhabdome inward. The shaft can reach a length of 850 μm and a diameter of 40 μm (*28*). In most locations along the main shaft, the morphology of the axial filament in cross section reveals a triangle-like shape and sometimes appears as a perfect triangle (inset in Fig. 1B). Finally, the third type is microscleres, called sterrasters, from *Geodia cydonium* (Linnaeus, 1767). Sterrasters densely populate the relatively thick cortex of the sponge. They are morphologically complex hyperbranched spherical spicules, up to 70 μm in diameter, that consist of numerous radially pointing arms originating from a common origin at the center of the spicule. Each branch contains an axial filament (*29*). Whereas the tips of these branches in mature sterrasters end with a flat spiny structure (Fig. 1C), the tips in immature spicules are sharp (Fig. 1D), and the triangular morphology of the inner axial filament is clearly observed (black triangles at the tips of the spicule, Fig. 1E).

To investigate the 3D spatial organization of axial filaments in these spicules, we used phase-contrast synchrotron-based computed tomography. The filaments comprising the megascleres of *T. aurantium* and *S. ponderosus* were imaged at the microtomography beamline (ID19), whereas a mature sterraster from *G. cydonium*, due to the relatively small diameter of its filaments, was imaged at the nanotomography beamline (ID16A-NI), both at the European Synchrotron Radiation Facility (ESRF) in Grenoble, France. Following the reconstruction of the morphology of the three spicules in 3D (Fig. 2, A, D, and G), we were able to track the internal organization of the axial filament within each spicule (Fig. 2, B, E, and H). In the case of *S. ponderosus*, only the branching portion of the entire spicule (Fig. 1B) is presented. On the basis of these results, it becomes evident that the proteinaceous filament contours the morphology of the spicules (Fig. 2, C, F, and I). However, to be able to correlate the shape of the filament with the crystallographic direction in which the branching occurs, information on the structure of the protein crystals comprising the filaments is required.

To study the crystalline properties of the axial filament in the three spicule types mentioned above, we performed an x-ray diffraction analysis using the small-angle x-ray scattering (SAXS) beamline (ID13) at the ESRF. Exceptionally sharp diffraction patterns collected from *T. aurantium* (Fig. 3A) and the main shaft of the megasclere in *S. ponderosus* (Fig. 3B) confirmed the highly regular single-crystalline nature of the axial filament in the spicules of these organisms. In both cases, by solving the diffraction patterns (figs. S1 and S2, respectively),

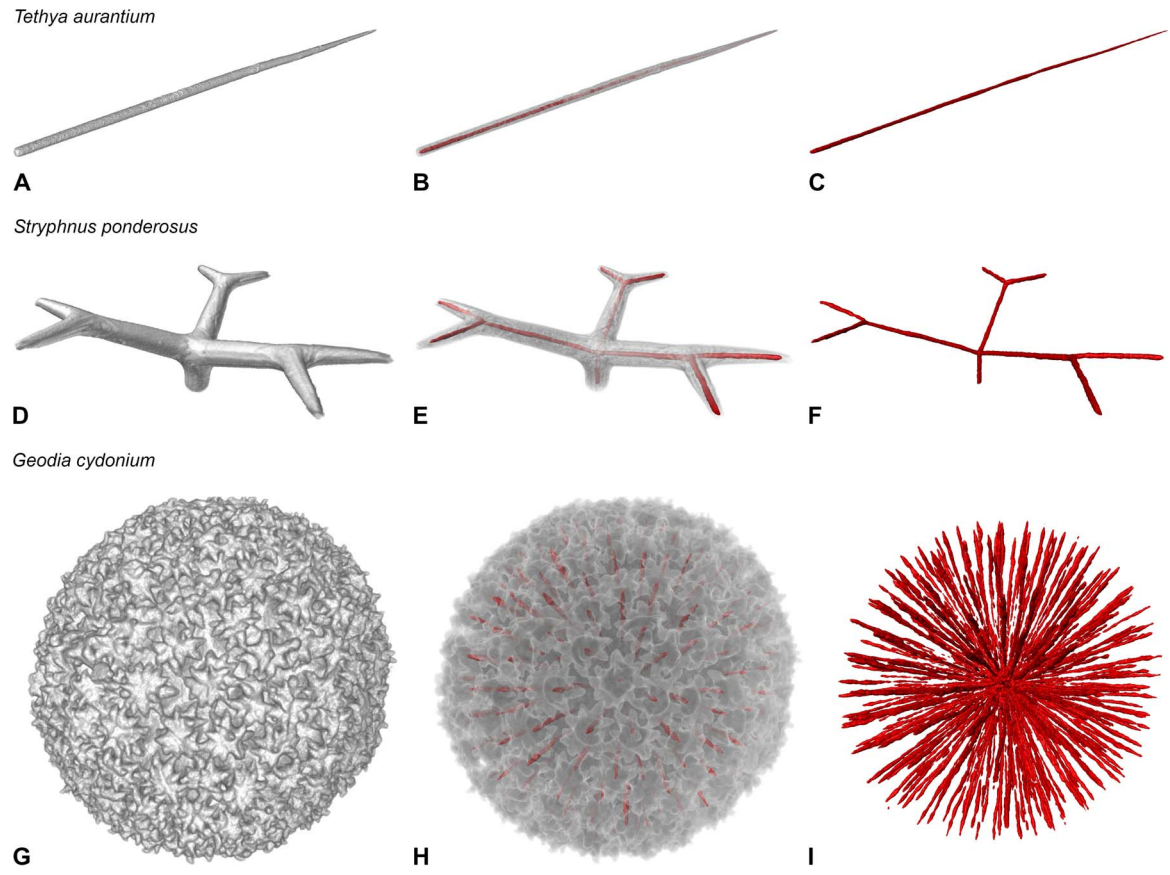


**Fig. 2. 3D morphology of demosponge spicules and their inner axial filaments as revealed by synchrotron microtomography and nanotomography.** A 3D reconstruction was obtained from the spicule, spicule plus the internal axial filament (red), and the filament alone in the demosponges (**A** to **C**) *T. aurantium*, (**D** to **F**) *S. ponderosus*, and (**G** to **I**) *G. cydonium*, respectively.

we find that the proteins are packed in a hexagonal crystal structure with lattice parameters of $a = 5.95 \pm 0.01$ nm and $c = 11.89 \pm 0.01$ nm in the case of *T. aurantium* and $a = 5.96 \pm 0.01$ nm and $c = 11.45 \pm 0.04$ nm in the case of *S. ponderosus*. Moreover, the long axis of the spicules is parallel to the *c* axis of the hexagonal lattice (the [001] direction). Because of structural complexity of the sterrasters from the demosponge *G. cydonium*, it was not possible to perform diffraction experiments on a single axial filament. Therefore, we used the x-ray setup to accumulate a diffraction signal while raster-scanning an entire mature spicule. Because the axial filaments in the sterraster point radially in all directions, we obtained a ring-like diffraction pattern characteristic of a polycrystalline material (Fig. 3C). Similar to the axial filaments in *T. aurantium* and *S. ponderosus*, the proteins in *G. cydonium* are packed in a hexagonal crystal structure with lattice parameters of $a = 5.93 \pm 0.01$ nm and $c = 11.97 \pm 0.05$ nm (fig. S3). These results agree with previous observations of Croce *et al.* (*12*, *13*), who used SAXS to investigate the periodicity of the proteinaceous axial filament in megascleres of a variety of demosponges. Their work proposed a hexagonal lattice with parameters of $a = 5.8$ nm and $c = 11.20$ nm in the case of *T. aurantium* (*12*) and $a = 5.8$ in the case of *G. cydonium* (*13*). A recent study used high-resolution transmission electron microscopy and scanning transmission electron microscopy to visualize the protein crystal within the axial filament in *T. aurantium* (*19*). Similar lattice parameters of $a = 5.6$ nm and $c = 11.20$ nm have been obtained.

It is intriguing that different spicules from three different organisms have almost identical crystallographic characteristics of the protein crystals comprising their axial filaments. At the same time, the spicules exhibit completely different morphologies with a varying degree of spatial complexity. The filament in the strongyloxea from *T. aurantium* shows no branching, which results in a needle-like morphology of the spicule (Fig. 2C), whereas the sterraster from *G. cydonium* is hyperbranched, developing a sphere-like morphology (Fig. 2I). At the same time, the axial filament in the dichotriaene from *S. ponderosus* shows a perfect threefold symmetry (Fig. 2F).

On the basis of the x-ray crystallographic data and the branching angles extracted from tomographic reconstructions (Fig. 4A), we propose a model that describes the crystallographic directions in which the spiculogenesis of the dichotriaene in *S. ponderosus* proceeds (Fig. 4B). Similar to the strongyloxea from *T. aurantium*, the filament in the main shaft of the spicule grows along the [001] direction, which is parallel to the vector of the reciprocal lattice $H = (001)$. The primary branching, which leads to the characteristic tetrapod shape, proceeds on crystallographic planes with the following Miller indices: $H_1 = (101)$, $H_2 = (0\bar{1}1)$, and $H_3 = (\bar{1}11)$. Note that these planes are related to each other by a sixfold symmetry. On the basis of the known lattice parameters, the angle between the main shaft ($H$ plane) and the branches ($H_i$ planes) is calculated as 65.73°, which is close to the mean value of 66.0° ± 2.0°, measured in the spicule. The calculated angle between the branches (that is, between vectors $H_i$) is 104.28°, which fits well to the mean measured value of 105.2° ± 1.6°. The secondary branching (fork-like in Fig. 1B) proceeds on crystallographic planes with the following Miller indices: $H_{11} = (261)$ and $H_{12} = (8\bar{6}1)$. The calculated angle between

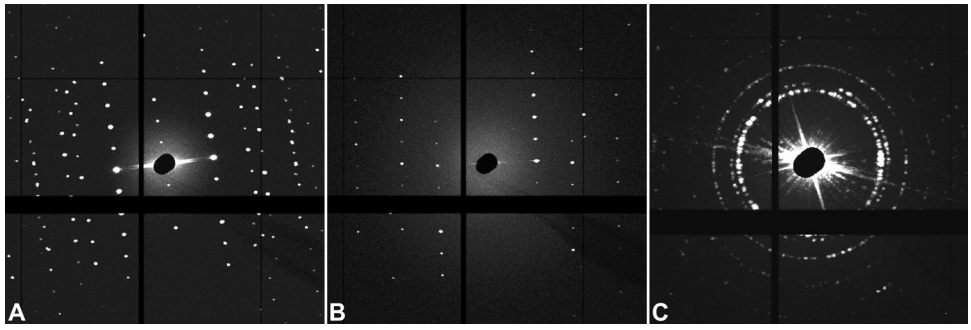


**Fig. 3. X-ray diffraction analysis of protein crystals comprising the axial filaments of demosponge spicules.** (**A**) X-ray diffraction pattern acquired from the strongyloxea from the demosponge *T. aurantium*. The pattern was obtained by accumulating the diffraction data while rotating the spicule around its long axis within an angular interval of 70°, the rotation axis being perpendicular to the incident beam. (**B**) X-ray diffraction pattern acquired from the main shaft of the dichotriaene from the demosponge *S. ponderosus*. The pattern was obtained by accumulating the diffraction data while rotating the spicule around the long axis of its main shaft within an angular interval of 70°, the rotation axis being perpendicular to the incident beam. (**C**) X-ray diffraction pattern acquired from a mature sterraster from the demosponge *G. cydonium*. The pattern was obtained by raster-scanning the entire spicule with the incident beam perpendicular to the rastering plane.

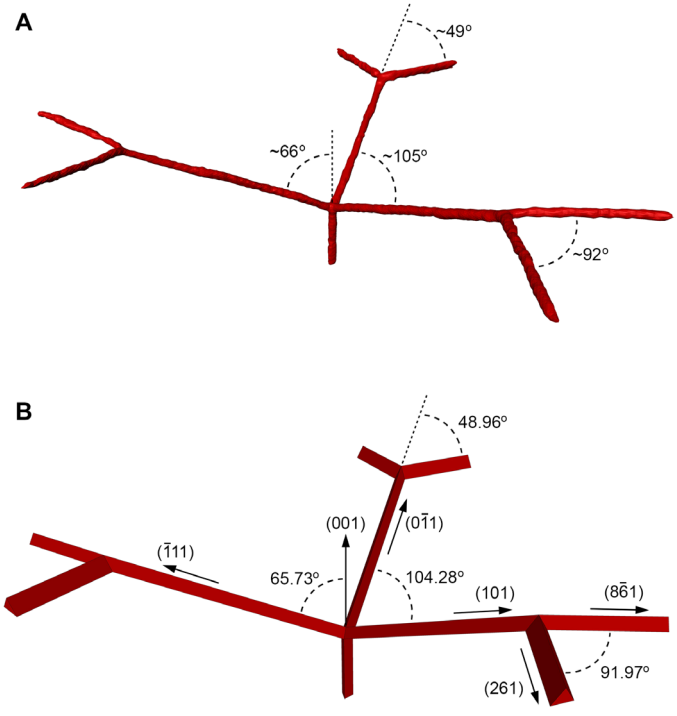


**Fig. 4. Proposed model of the morphogenesis of a dichotriaene in *S. ponderosus*.** (**A**) Angles between the different branches in the dichotriaene extracted from the x-ray microtomography reconstruction. (**B**) Three-dimensional model of the axial filament in dichotriaene and the Miller indices of the leading crystallographic planes in the branches, which were deduced from the crystal structure of the filament and the measured angles between branches. The numerical values are the angles between branches calculated with the aid of the lattice parameters of the mesoscopic protein crystal comprising the axial filament.

the corresponding tripod component ($H_1$) and a secondary branch ($H_{11}$ or $H_{12}$) is 48.96°, whereas the average of the measured angle is 48.7° ± 1.5°. The calculated angle between the secondary branches ($H_{ij}$) is 91.97° versus the measured value of 92.4° ± 1.9°. The branching model of the filament in *S. ponderosus* is schematically depicted in Fig. 4B.

## DISCUSSION

Our study uncovers a half-a-billion-year-old fabrication concept that only recently has been used by mankind to produce novel materials for the use in solar cells, plasmonics, optoelectronics, and sensing (*20*–*25*). The described growth mechanism uses similar branching principles that are used in the synthesis of abiotic inorganic nanocrystals and thus provides insights into the origins of morphological symmetry in these complex biological organisms. Despite the fact that the different entities, in the biological and the synthetic systems, have identical crystallographic characteristics, their growth results in a diversity of linear, branched, and hyperbranched morphologies. In the spicules of Demospongiae, the branching of the axial filament is most probably orchestrated by the cellular component, the sclerocytes, and is therefore genetically controlled. In contrast, the branching in the synthetic system is controlled by the physical and chemical properties of the growth medium (*24*, *25*). Nevertheless, in both cases, it proceeds in specific crystallographic directions of the protein or the atomic lattice. To conclude,

we find it fascinating that nature and mankind independently converged to a similar route of forming highly regular 3D architectures. Using the crystalline axial filament, nature has mastered the fabrication of extremely complex glass structures at low temperatures—a capacity that is far beyond the reach of current human technology. Further understanding of how the organisms regulate the branching events in the filaments has the potential to be adopted in the production of technologically relevant nanocrystalline materials.

## MATERIALS AND METHODS

### Sample preparation

Specimens of the sponges were treated with 5% (v/v) sodium hypochlorite solution until all the organic material surrounding the spicules was removed. The residual mass containing the spicules was rinsed five times with Milli-Q water and two times with 95% ethanol and finally air-dried.

### Electron microscopy

The spicules were mounted on a carbon tape and imaged with a Scios field-emission dual-beam electron microscope (FEI) using secondary electrons at 2 kV and 25 pA. Cross sections of the spicule samples were prepared by conventional FIB milling at 30 kV and using different current-defining apertures. To avoid charging of the cross sections, the low-vacuum option (0.3-mbar $H_2O$) for imaging of the spicules was used.

### Synchrotron x-ray microtomography

The 3D spatial arrangement of the axial filaments in the spicules from *T. aurantium* and *S. ponderosus* was imaged at the microtomography beamline ID19 of the ESRF. The samples were scanned using an x-ray photon energy of 26.3 keV at a sample-detector distance of 20 mm. A total of 4000 radiographic projection images were recorded over 180° with an exposure time of 0.1 s and an effective pixel size of 0.647 µm. A so-called single-harmonic undulator was used to allow for a narrow bandwidth of the radiation impinging on the sample in pink-beam mode. ESRF in-house code (PyHST2) was used to reconstruct the data. Simple back projection reconstructions and single-distance phase-retrieved versions of each data set were used to facilitate automated data processing and segmentation. The organic filament was enhanced by means of Paganin's approach with a δ/β ratio of 300. The reconstructed 3D volumes were visualized and rendered with the 3D visualization software Avizo 9.2 (FEI).

### Synchrotron x-ray nanotomography

Projection phase-contrast nanotomography measurements of the spicules in *G. cydonium* were conducted at the ID16A-NI nano-imaging beamline of the ESRF. A pair of multilayer-coated Kirkpatrick-Baez optics was used to focus the x-rays at 33.6 keV into a spot of approximately 20 nm. The sample was placed on a rotation stage downstream the focal spot, and holograms were recorded at four distances between the focal plane and the detector. For each tomographic angle, the four holograms were combined to retrieve phase maps, which were then used to reconstruct tomograms via filtered back projection (PyHST2). The pixel size was set to 100 nm, and 1800 angular projections were acquired for each propagation distance with an exposure time of 1 s. The reconstructed 3D volumes were visualized and rendered with the 3D visualization software Avizo 9.2 (FEI).

### Synchrotron x-ray diffraction

X-ray nanodiffraction experiments of the spicule samples were performed at the ID13 nanofocus beamline of the ESRF. The measurements were conducted in transmission geometry using photons with an energy of 14.85 keV (λ = 0.8349 Å). The footprint of the beam on the sample of 200 nm × 200 nm (full width at half maximum) was achieved using silicon-based compound refractive lenses with a focal distance of 14 mm and an acceptance of less than 20 µm. The scattering signal was recorded with an EIGER 4M detector (Dectris Ltd.) at a sample-detector distance of 494 mm, as calibrated using silver behenate as reference. During the measurement of a sterraster from *G. cydonium*, the spicules (area, 50 µm × 50 µm) were raster-scanned perpendicular to the incident beam with a step size of 500 nm using an acquisition time of 0.3 s per point. Diffraction patterns of a strongyloxea from *T. aurantium* and a dichotriaene from *S. ponderosus* were measured using linear raster scans across the spicules at various angles of incidence. The spicules were rotated around their long axis perpendicular to the incident beam within an angular range of 70°. Line scan measurements were conducted at intervals of 0.25° using an acquisition time of 0.5 s per point. The diffraction data were analyzed using FIT2D software.

## SUPPLEMENTARY MATERIALS

Supplementary material for this article is available at http://advances.sciencemag.org/cgi/content/full/3/10/eaao2047/DC1

fig. S1. Indexed x-ray diffraction pattern acquired from the strongyloxea from the demosponge *T. aurantium*.

fig. S2. Indexed x-ray diffraction pattern acquired from the main shaft of the dichotriaene from the demosponge *S. ponderosus*.

fig. S3. Indexed x-ray diffraction pattern acquired from a mature sterraster from the demosponge *G. cydonium*.

## REFERENCES AND NOTES


1. M.-J. Uriz, Mineral skeletogenesis in sponges. *Can. J. Zool.* **84**, 322–356 (2006).
2. H. C. Schröder, X. Wang, W. Tremel, H. Ushijima, W. E. G. Müller, Biofabrication of biosilica-glass by living organisms. *Nat. Prod. Rep.* **25**, 455–474 (2008).
3. M.-J. Uriz, X. Turon, M. A. Becerro, G. Agell, Siliceous spicules and skeleton frameworks in sponges: Origin, diversity, ultrastructural patterns, and biological functions. *Microsc. Res. Tech.* **62**, 279–299 (2003).
4. R. W. M. van Soest, E. J. Beglinger, Tetractinellid and hadromerid sponges of the sultanate of Oman. *Zool. Meded.* **82**, 749–790 (2008).
5. A. Plotkin, C. Morrow, E. Gerasimova, H. T. Rapp, Polymastiidae (Demospongiae: Hadromerida) with ornamented exotyles: A review of morphological affinities and description of a new genus and three new species. *J. Mar. Biol. Assoc. UK* 1351–1406 (2017).
6. J. C. Weaver, D. E. Morse, Molecular biology of demosponge axial filaments and their roles in biosilicification. *Microsc. Res. Tech.* **62**, 356–367 (2003).
7. J. N. Cha, K. Shimizu, Y. Zhou, S. C. Christiansen, B. F. Chmelka, G. D. Stucky, D. E. Morse, Silicatein filaments and subunits from a marine sponge direct the polymerization of silica and silicones in vitro. *Proc. Natl. Acad. Sci.* **96**, 361–365 (1999).
8. V. V. Annenkov, E. N. Danilovtseva, Spiculogenesis in the siliceous sponge *Lubomirskia baicalensis* studied with fluorescent staining. *J. Struct. Biol.* **194**, 29–37 (2016).
9. X. Wang, H. C. Schröder, K. Wang, J. A. Kaandorp, W. E. G. Müller, Genetic, biological and structural hierarchies during sponge spicule formation: From soft sol–gels to solid 3D silica composite structures. *Soft Matter* **8**, 9501–9518 (2012).
10. T. L. Simpson, P.-F. Langenbruch, L. Scalera-Liaci, Silica spicules and axial filaments of the marine sponge *Stelletta grubii* (Porifera, Demospongiae). *Zoomorphology* **105**, 375–382 (1985).
11. H. M. Reiswig, Axial symmetry of sponge spicules and its phylogenetic significance. *Cah. Biol. Mar.* **12**, 505–514 (1971).
12. G. Croce, D. Viterbo, M. Milanesio, H. Amenitsch, A mesoporous pattern created by nature in spicules from *Thetya aurantium* sponge. *Biophys. J.* **92**, 288–292 (2007).

13. G. Croce, A. Frache, M. Milanesio, D. Viterbo, G. Bavestrello, U. Benatti, M. Giovine, H. Amenitsch, Fiber diffraction study of spicules from marine sponges. *Microsc. Res. Tech.* **62**, 378–381 (2003).
14. D. F. Travis, C. J. François L. C. Bonar, M. J. Glimcher, Comparative studies of the organic matrices of invertebrate mineralized tissues. *J. Ultrastruct. Res.* **18**, 519–550 (1967).
15. R. Garrone, Collagène, spongine et squelette minèral chez l'èponge *Haliclona rosea* (O.S.) (Dèmosponge, Haplosclèride). *J. Microsc.* **8**, 581–598 (1969).
16. I. Zlotnikov, P. Werner, H. Blumtritt, A. Graff, Y. Dauphin, E. Zolotoyabko, P. Fratzl, A perfectly periodic three-dimensional protein/silica mesoporous structure produced by an organism. *Adv. Mater.* **26**, 1682–1687 (2014).
17. M. J. Uriz, X. Turon, M. A. Becerro, Silica deposition in Demosponges: Spiculogenesis in *Crambe crambe*. *Cell Tissue Res.* **301**, 299–309 (2000).
18. I. Zlotnikov, P. Werner, P. Fratzl, E. Zolotoyabko, Eshelby twist as a possible source of lattice rotation in a perfectly ordered protein/silica structure grown by a simple organism. *Small* **11**, 5636–5641 (2015).
19. P. Werner, H. Blumtritt, F. Natalio, Organic crystal lattices in the axial filament of silica spicules of Demospongiae. *J. Struct. Biol.* **198**, 186–195 (2017).
20. D. Deng, J. Wang, J.-S. Yu, Planar Se multipod crystals with unusual growth directions: Thoughts on the spontaneous growth of hexagonal Se. *CrstEngComm* **17**, 4349–4354 (2015).
21. S. Chen, Z. L. Wang, J. Ballato, S. H. Foulger, D. L. Carroll, Monopod, bipod, tripod, and tetrapod gold nanocrystals. *J. Am. Chem. Soc.* **125**, 16186–16187 (2003).
22. H. Li, A. G. Kanaras, L. Manna, Colloidal branched semiconductor nanocrystals: State of the art and perspectives. *Acc. Chem. Res.* **46**, 1387–1396 (2013).
23. D. J. Milliron, S. M. Hughes, Y. Cui, L. Manna, J. Li, L.-W. Wang, A. P. Alivisatos, Colloidal nanocrystal heterostructures with linear and branched topology. *Nature* **430**, 190–195 (2004).
24. A. G. Kanaras, C. Sönnichsen, H. Liu, A. P. Alivisatos, Controlled synthesis of hyperbranched inorganic nanocrystals with rich three-dimensional structures. *Nano. Lett.* **5**, 2164–2167 (2005).
25. L. Manna, D. J. Milliron, A. Meisel, E. C. Scher, A. P. Alivisatos, Controlled growth of tetrapod-branched inorganic nanocrystals. *Nat. Mater.* **2**, 382–385 (2003).
26. M. A. Monn, H. Kesari, A new structure-property connection in the skeletal elements of the marine sponge *Tethya aurantia* that guards against buckling instability. *Sci. Rep.* **7**, 39547 (2017).
27. G. Bavestrello, B. Calcinai, L. Ceccati, C. Cerrano, M. Sara, Skeletal development in two species of *Tethya* (Porifera, Demospongiae). *Ital. J. Zool.* **67**, 241–244 (2000).
28. W. A. Arndt, in *Die Tierwelt der Nord und Ostsee*, G. Grimpe, E. Wagler, Eds. (Akademische Verlagsgesellschaft, 1935), pp. 1–140.
29. X. Wang, M. Wiens, U. Schloßmacher, K. P. Jochum, H. C. Schröder, W. E. G. Müller, Bio-sintering/bio-fusion of silica in sponge spicules. *Adv. Eng. Mater.* **14**, B4–B12 (2012).

**Acknowledgments:** We thank the ESRF for beam time allocation on beamlines ID13, ID16A, and ID19. **Funding:** This work was supported by Bundesministerium für Bildung und Forschung through grant 03Z22EN11. **Author contributions:** I.Z. conceived the study, designed and performed all the experiments, analyzed the data, and wrote the paper. V.S. performed the microtomography and diffraction experiments and segmented all the 3D data. P.Z., A.P., and A.R. performed the microtomography and nanotomography experiments. E.Z. provided expertise in diffraction data analysis. E.R. performed the electron microscopy. M.R. performed the diffraction experiments. J.V. provided the spicule samples. All authors commented on the manuscript. **Competing interests:** The authors declare that they have no competing interests. **Data and materials availability:** All data needed to evaluate the conclusions in the paper are present in the paper and/or the Supplementary Materials. Additional data related to this paper may be requested from the authors.

Submitted 26 June 2017
Accepted 21 September 2017
Published 18 October 2017
10.1126/sciadv.aao2047

**Citation:** V. Schoeppler, E. Reich, J. Vacelet, M. Rosenthal, A. Pacureanu, A. Rack, P. Zaslansky, E. Zolotoyabko, I. Zlotnikov, Shaping highly regular glass architectures: A lesson from nature. *Sci. Adv.* **3**, eaao2047 (2017).

# Shaping highly regular glass architectures: A lesson from nature

Vanessa Schoeppler, Elke Reich, Jean Vacelet, Martin Rosenthal, Alexandra Pacureanu, Alexander Rack, Paul Zaslansky, Emil Zolotoyabko and Igor Zlotnikov

*Sci Adv* **3** (10), eaao2047.
DOI: 10.1126/sciadv.aao2047